

SCIENTIFIC REPORTS



OPEN

Small-window parametric imaging based on information entropy for ultrasound tissue characterization

Po-Hsiang Tsui^{1,2,3}, Chin-Kuo Chen⁴, Wen-Hung Kuo⁵, King-Jen Chang^{5,6}, Jui Fang⁷, Hsiang-Yang Ma¹ & Dean Chou⁸

Received: 14 April 2016
Accepted: 15 November 2016
Published: 20 January 2017

Constructing ultrasound statistical parametric images by using a sliding window is a widely adopted strategy for characterizing tissues. Deficiency in spatial resolution, the appearance of boundary artifacts, and the prerequisite data distribution limit the practicability of statistical parametric imaging. In this study, small-window entropy parametric imaging was proposed to overcome the above problems. Simulations and measurements of phantoms were executed to acquire backscattered radiofrequency (RF) signals, which were processed to explore the feasibility of small-window entropy imaging in detecting scatterer properties. To validate the ability of entropy imaging in tissue characterization, measurements of benign and malignant breast tumors were conducted ($n = 63$) to compare performances of conventional statistical parametric (based on Nakagami distribution) and entropy imaging by the receiver operating characteristic (ROC) curve analysis. The simulation and phantom results revealed that entropy images constructed using a small sliding window (side length = 1 pulse length) adequately describe changes in scatterer properties. The area under the ROC for using small-window entropy imaging to classify tumors was 0.89, which was higher than 0.79 obtained using statistical parametric imaging. In particular, boundary artifacts were largely suppressed in the proposed imaging technique. Entropy enables using a small window for implementing ultrasound parametric imaging.

Ultrasound backscattering and its relationship with the properties of scatterers in biological tissues is a widely pursued and critical topic in fundamental imaging research. In ultrasound imaging, the speckle results from the accumulation of random scatterings from within the resolution cell of the transducer^{1,2}. On the basis of the randomness of ultrasound backscattered signals, backscattered envelope statistics (i.e., the echo amplitude distribution) can be modeled using mathematical statistical distributions to evaluate scatterer properties. Several statistical models have been proposed to describe the backscattered statistics for ultrasound tissue characterization, such as Rayleigh², Rician³, K^4 , homodyned K^5 , generalized K^6 , Nakagami⁷, Nakagami compounding^{8–10}, and McKay distributions¹¹. General models that fit closely with different statistical distributions of backscattered envelopes are highly necessary.

Among the aforementioned models, the Nakagami distribution is the most frequently adopted model for tissue characterization because of its generality, simplicity, and low computational complexity¹². Researchers reported potential applications of ultrasound Nakagami parametric imaging in visualizing backscattered statistics for quantifying the properties of tissues, such as in breast tumor classification^{13,14}, liver fibrosis detection in rats^{15,16}, radiotherapy evaluation¹⁷, cataract detection¹⁸, skin characterization¹⁹, vascular flow analysis²⁰, thermal ablation monitoring²¹, and characterizing the structural anisotropy in the myocardium²². Various research groups

¹Department of Medical Imaging and Radiological Sciences, College of Medicine, Chang Gung University, Taoyuan, Taiwan. ²Medical Imaging Research Center, Institute for Radiological Research, Chang Gung University and Chang Gung Memorial Hospital at Linkou, Taoyuan, Taiwan. ³Department of Medical Imaging and Intervention, Chang Gung Memorial Hospital at Linkou, Taoyuan, Taiwan. ⁴Department of Otolaryngology–Head and Neck Surgery, Chang Gung Memorial Hospital and Chang Gung University, Taoyuan, Taiwan. ⁵Department of Surgery, National Taiwan University Hospital, Taipei, Taiwan. ⁶Taiwan Breast Cancer Foundation, Taipei, Taiwan. ⁷Ph.D. Program in Biomedical Engineering, College of Engineering, Chang Gung University, Taoyuan, Taiwan. ⁸Institute of Biomedical Engineering & Department of Engineering Science, University of Oxford, Oxford, UK. Correspondence and requests for materials should be addressed to P.-H.T. (email: tsuihp@mail.cgu.edu.tw)

demonstrated that the Nakagami image visualizes scatterer arrangements and concentrations and complements the conventional B-scan for tissue characterization.

Low spatial resolution is a substantial drawback of using statistical parameters, including the Nakagami parameter, to image tissues. The sliding window technique is a typical method for constructing ultrasound statistical parametric images^{18–25}. A window within the image is used to collect local data for estimating a parameter; this estimation is repeated as the window is moved across the image, yielding a statistical parametric map. The window size determines the resolution of the parametric image: a smaller window offers a higher resolution. However, to avoid overestimating the statistical parameter, a window with a size corresponding to several times the spatial resolution of the B-scan is used to capture sufficient data points for calculation^{26,27}. Hence, the resolution of statistical parametric images is lower than that of the conventional B-scan. In addition to low image resolution, ultrasound statistical parametric images entail another practical challenge: the data acquired for parameter estimation must follow the employed distribution model^{28,29}. Not every imaging system outputs raw radiofrequency (RF) data of images. Adjusting the settings of an ultrasound system or using signal processing techniques may also alter the statistical distribution of the image data obtained from the system. In particular, different demodulation methods may cause different envelope statistics³⁰, and different estimators yield different estimates³¹. These aspects highlight the lack of flexibility in applying statistical distributions to ultrasound parametric imaging.

Information entropy has a high potential for application in analyzing ultrasound backscattering. Shannon established a mathematical theory of communication and defined entropy as a measure of uncertainty in a random variable³². Hughes first proposed using information Shannon entropy for analyzing ultrasound signals and demonstrated that entropy can quantitatively describe microstructural changes in scattering media^{33–36}. To visualize changes in the uncertainty of backscattered signals, ultrasound entropy imaging techniques were further developed^{37–40}. Note that entropy is a function of probability density and thus is related to the distribution parameters²⁸. However, the difference is that entropy is a relative measure of the signal uncertainty (a non-model-based statistical parameter) and therefore can be calculated using any type of data irrespective of the data distribution. In this case, using a large window to involve sufficient data points for a stable entropy calculation may be not a very critical consideration. We assume that using entropy affords the use of a small window for constructing high-resolution ultrasound parametric images. Using information entropy as a strategy for ultrasound small-window parametric imaging has not been explored previously.

In this study, we aim to (i) design an algorithmic scheme for ultrasound entropy imaging, (ii) investigate the feasibility of small-window entropy imaging in reflecting the scatterer properties, and (iii) validate the practical ability of small-window entropy imaging in tissue characterization by clinical measurements on breast tumors and comparisons with statistical parametric imaging based on the Nakagami distribution. The results showed that information entropy can be used to implement small-window parametric imaging (window side length (SL) = 1 transducer pulse length) and to provide high-resolution images that visualize the uncertainty of backscattered RF signals for characterizing tissues. Compared with Nakagami parametric imaging, small-window entropy imaging improved the performance of breast tumor classification. This paper reports the potential contributions, impacts, and future work of entropy imaging in ultrasound tissue characterization.

Results

Simulations and phantom experiments were conducted to explore the feasibility of small-window entropy imaging. Different types of phantoms were designed and the properties and materials of each type of phantom in the simulations and experiments are shown in Table 1. To confirm the practical performance of small-window entropy imaging in tissue characterization, clinical data of breast benign (fibroadenoma) and malignant (invasive carcinoma) tumors were further collected for validations.

Simulations. Figure 1 shows B-mode and entropy images of Type-I phantoms obtained using SLs of 1 to 4. The entropy image varied from blue–red-interlaced to red, which represents an increase in entropy, as the number density of scatterers increased from 2 to 16 scatterers/mm². Figure 2 shows the entropy values as a function of SL at different number densities of scatterers. At each scatterer concentration, the estimated entropy decreased with increasing SL. Figure 3 shows entropy as a function of the number density of the scatterers obtained at different SLs. The entropy estimated from the entropy image constructed using SL = 1 increased from 5.17 ± 0.01 to 5.35 ± 0.005 as the number density of scatterers increased from 2 to 16 scatterers/mm². This phenomenon was also observed for an SL of 2–4. Interestingly, entropy images constructed using a small window (SL = 1) can detect the variation in the number density of scatterers in a scattering medium.

Figure 4 presents B-mode and entropy images of Type-II phantoms containing strong scatterers with different relative scattering coefficients (RSCs) constructed using different SLs. For SL = 1–4, the entropy image varied from red to red–blue-interlaced, which represents a decrease in entropy, as the RSC of the embedded strong scatterers increased from 2 to 8. Figure 5 presents entropy as a function of the RSC of the embedded strong scatterers when different SLs were used. As the RSC of the strong scatterers increased from 2 to 8, entropy in the image constructed using SL = 1 decreased from 5.34 ± 0.004 to 5.20 ± 0.009 . Entropies obtained using SLs of 2–4 also decreased with increasing RSCs. The results showed that small-window entropy imaging (SL = 1) allows quantification of the tissue inhomogeneity.

Figure 6(a–d) show B-mode and entropy images of a simulated mass (Type-III phantom) obtained using different window sizes. In the entropy image, the background and the mass had the same number density of scatterers but different RSCs. A blue image feature appeared at the background–mass interface (boundary artifact). The boundary artifact was conspicuous when windows with a large SL were used, and it gradually diminished as the SL decreased from 4 to 1. According to the above findings, the following results from the phantoms and clinical measurements were obtained using SL = 1 to investigate small-window entropy imaging in practical applications.

	Type no.	Objectives	Properties of the scatterers in the background	Additional scatterers or additive in the background
Simulations	Type-I	Simulating changes in the number density of scatterers	Point scatterers (RSC: 1) Number density of scatterers: 2, 4, 8, and 16 scatterers/mm ²	—
	Type-II	Simulating changes in the degree of variance in the echogenicity	Point scatterers (RSC: 1) Number density of scatterers: 16 scatterers/mm ²	Point scatterers (RSC: 2, 4, 6, and 8) Number density of scatterers: 1 scatterers/mm ²
	Type-III	Simulating the tissue interface	Point scatterers (RSC: 1) Number density of scatterers: 16 scatterers/mm ²	An embedded cylindrical object with point scatterers (RSC: 0.1) Number density of scatterers: 16 scatterers/mm ²
Phantom experiments	Type-A	Simulating changes in the number density of scatterers	Glass beads Number density of scatterers: 2, 4, 8, and 16 scatterers/mm ³	—
	Type-B	Simulating changes in the degree of variance in the echogenicity	Graphite powder Scatterer concentration: 2 g in 200 mL water (>1000 scatterers/mm ³)	Glass beads Scatterer concentration: 0.05, 0.1, and 0.3 g in 200 mL water
	Type-C	Simulating the attenuation effect	Graphite powder Scatterer concentration: 2 g in 200 mL water (>1000 scatterers/mm ³)	Soybean-oil lipid emulsions Lipid concentration: 0%, 5%, 10%, and 20%
	Type-D	Simulating the tissue interface and exploring effects of frequency and focus	A tissue-mimicking breast phantom	—

Table 1. Properties and materials of each type of phantom in the simulations and experiments. RSC: Relative scattering coefficients of scatterers in the simulations. The phantoms were constructed by boiling and cooling agar–water mixtures (dissolving 3 g of the agar powder into 200 mL of water) and adding different materials, including glass beads with diameters of 75 μm (Model 59200U, Supelco, Bellefonte, PA, USA), graphite powder with diameters < 20 μm (Model 282863, Sigma-Aldrich, St. Louis, MO, USA), and soybean-oil lipid emulsions (Intrafat, Nihon Pharmaceutical Industry, Osaka, Japan). In the simulations and phantom experiments, scatterers were randomly distributed.

Phantom experiments. Figure 7 shows the B-mode and small-window entropy images of the Type-A phantom (frequency = 6 MHz; scanned at a focus of 1 cm). The entropy increased from 4.41 ± 0.07 to 5.00 ± 0.03 as the number density of scatterers increased from 2 to 16 scatterers/mm³. The results obtained from Type-A phantoms showed a similar trend with that of Type-I phantoms, indicating that entropy imaging can be used to visualize the variation in the number density of scatterers. Figure 8 displays the B-mode and small-window entropy images of the Type-B phantom (frequency = 6 MHz; scanned at a focus of 1 cm). The entropy decreased from 5.12 ± 0.02 to 4.91 ± 0.02 as the weights of the glass beads added in the background increased from 0 to 0.3 g. The experimental results for the Type-B phantoms confirmed the findings of the simulations of the Type-II phantoms: entropy allows the quantification of the tissue inhomogeneity.

Figure 9(a–h) show the B-mode and small-window entropy images of the Type-C phantom (frequency = 6 MHz; scanned at a focus of 1 cm). Figure 9(i–l) illustrate the envelope amplitude values as functions of depth obtained by averaging all the envelope signals in Fig. 9(a–d), respectively. At a lipid concentration of 20%, the average attenuation rate for envelope signals was 2.56/mm, which was determined by the slope of the linear fitting curve. Figure 9(m–p) indicate that the average attenuation rate for the entropy image at a lipid concentration of 20% was 0.0008/mm, which is much lower than that of the B-scan.

Figure 10(a–j) display the B-mode and small-window entropy images of the Type-D phantom obtained using frequencies ranging from 5 to 8 MHz (scanned at a focus of 2 cm). Figure 10(k–l) show the results determined using a frequency of 6 MHz and a focal length of 3 cm (the mass was not located in the focal zone). Refer to Fig. 10(m). According to the *p* value obtained from the independent *t* test, increasing the frequency from 5 to 8 MHz did not result in a significant change in entropy, but the entropy estimated in the focal zone was lower than that obtained when the focal zone was moved away from the mass (*p* value < 0.05, denoted by the “*” symbol in the figure).

Clinical data of breast tumor. Figure 11 provides the B-mode, Nakagami, and small-window entropy images of benign and malignant breast tumors. The shade of the Nakagami and entropy images of the malignant tumor was darker than that of the benign tumor. Figure 12(a) shows that the median Nakagami parameter for the benign and malignant tumors was 0.59 (the interquartile range, IQR: 0.46–0.67) and 0.38 (IQR: 0.25–0.53), respectively (*p* < 0.05). Figure 12(b) displays the receiver operating characteristic (ROC) curve for using the Nakagami image to classify the benign and malignant tumors. The area under the ROC curve (AUROC) was 0.79 with a 95% confidence interval (CI) from 0.67 to 0.9. The accuracy was 69.84%, the sensitivity was 70%, and the specificity was 69.69%. Concurrently, the median entropy for the benign and malignant tumors, as shown in Fig. 12(c), was 4.86 (IQR: 4.57–4.96) and 4.29 (IQR: 3.87–4.51), respectively (*p* < 0.05). The AUROC for entropy imaging was 0.89 (95% CI: 0.80 to 0.97), and the accuracy was 79.36%, the sensitivity was 76.66%, and the specificity was 81.81%, as shown in Fig. 12(d). Table 2 compares performances of ultrasound small-window entropy and Nakagami imaging in classifying breast tumors. Compared with statistical parametric imaging constructed using a relatively large sliding window, small-window entropy imaging improved the performance of breast tumor classification.

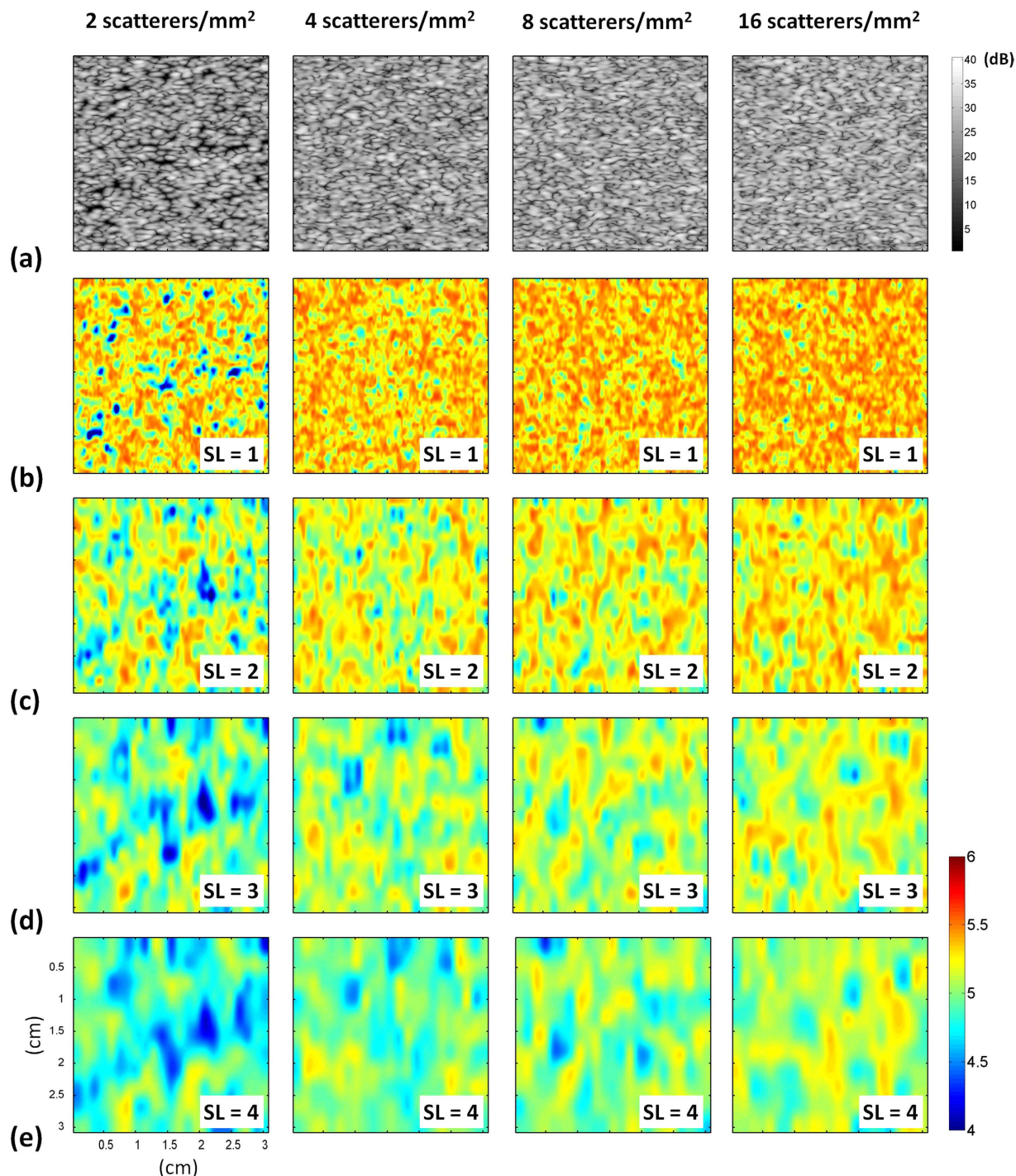


Figure 1. (a) B-mode and (b–e) entropy images of Type-I simulated phantoms with different number densities of scatterers. (b) SL = 1; (c) SL = 2; (d) SL = 3; (e) SL = 4. The dimensions for all images are the same. The grayscale and color bars represent the pixel values (the brightness) of the B-mode and entropy images, respectively. The shade of the entropy image depends on the window size.

Discussion

Significance of this study. This paper presents solutions to the problems associated with ultrasound statistical parametric imaging for visualizing the information associated with tissue microstructures. According to the simulation, phantom, and clinical measurement results obtained in this study, ultrasound entropy imaging is superior to statistical parametric mapping in the following aspects: (i) Small-window entropy images constructed using SL = 1 effectively describe the changes in scatterer properties. Compared with statistical parametric images, entropy images characterize tissues without sacrificing the resolution. (ii) Boundary artifacts occur at the interface when using sliding windows to construct parametric images. Because using entropy enables using a small

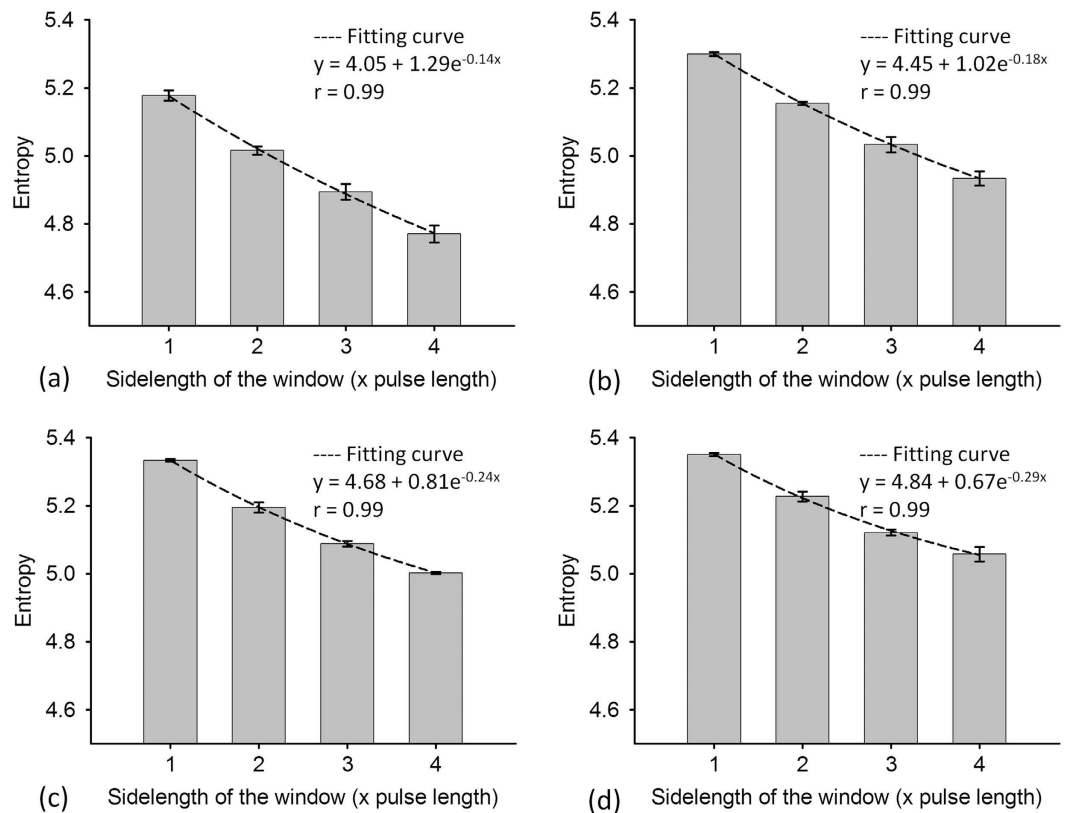


Figure 2. Simulated entropy values as a function of SL at different number densities of scatterers.

(a) 2 scatterers/mm²; (b) 4 scatterers/mm²; (c) 8 scatterers/mm²; (d) 16 scatterers/mm². At each scatterer concentration, the estimated entropy decreased with increasing SL. Data were expressed by mean \pm standard deviation.

window for parametric imaging, the effects of boundary artifacts are largely suppressed to improve the performance of tissue characterization. This is the first to demonstrate the usefulness of small-window entropy imaging in ultrasound tissue characterization.

Effects of scatterer arrangements on entropy. Establishing a physical link between information entropy and the tissue microstructure is highly necessary for clinical applications. Clinically, normal soft tissue parenchyma, such those of the liver⁴¹ and breast⁴², may be treated as homogeneous media with a considerable number of randomly distributed scatterers. A change in the scatterer arrangement, from homogeneous to inhomogeneous, of a scattering medium may be used to explain the pathological change of a soft tissue from the normal to the abnormal stage. Our simulation and phantom results clarified the dependency of information entropy on scatterer properties (Figs 1, 2, 3, 4, 5, 7 and 8). In homogeneous media, entropy is determined by the number of scatterers. Increasing the number density of scatterers represents that more scatterers interact with the incident wave, thus complicating wave interference and generating backscattered signals with different amplitudes corresponding to high entropies (the signal uncertainty). In inhomogeneous media, a relatively high degree of variance in the scattering cross sections of the scatterers causes local variance in the amplitude of the RF signal waveform, thus narrowing the width of the signal probability distribution $w(y)$; this condition reduces the estimated value of entropy.

Effects of attenuation, frequency, and focus on entropy. It has been shown that entropy estimated using the probability distribution of ultrasound signals is proportional to ultrasound statistical parameters, and therefore it is expected to inherit the properties of statistical parameters, such as the dependencies of number density of scatterers, attenuation, noise, frequency, transducer focusing, and other factors that affect the size of the resolution cell⁴³. The effects of number density of scatterers on entropy were discussed in the previous paragraph. The results showed that entropy value decreases with depth due to attenuation (Fig. 9), as supported by a recent report revealing that decreasing the signal amplitude with depth decrease statistical parameters⁴⁴. The attenuation effect reduces the signal-to-noise ratio (SNR). Under a low SNR, noise typically behaves as a random variable with Gaussian distribution of zero mean, and the coupling of noise with backscattered echoes tends to change the signal amplitude distribution and the corresponding statistical parameters. Although the minimum requirement of a threshold SNR for entropy estimation is unknown currently, a previous study reported that estimations of statistical parameters can be stable and reach a steady state for SNRs above 20 dB, whereas the parameter estimation

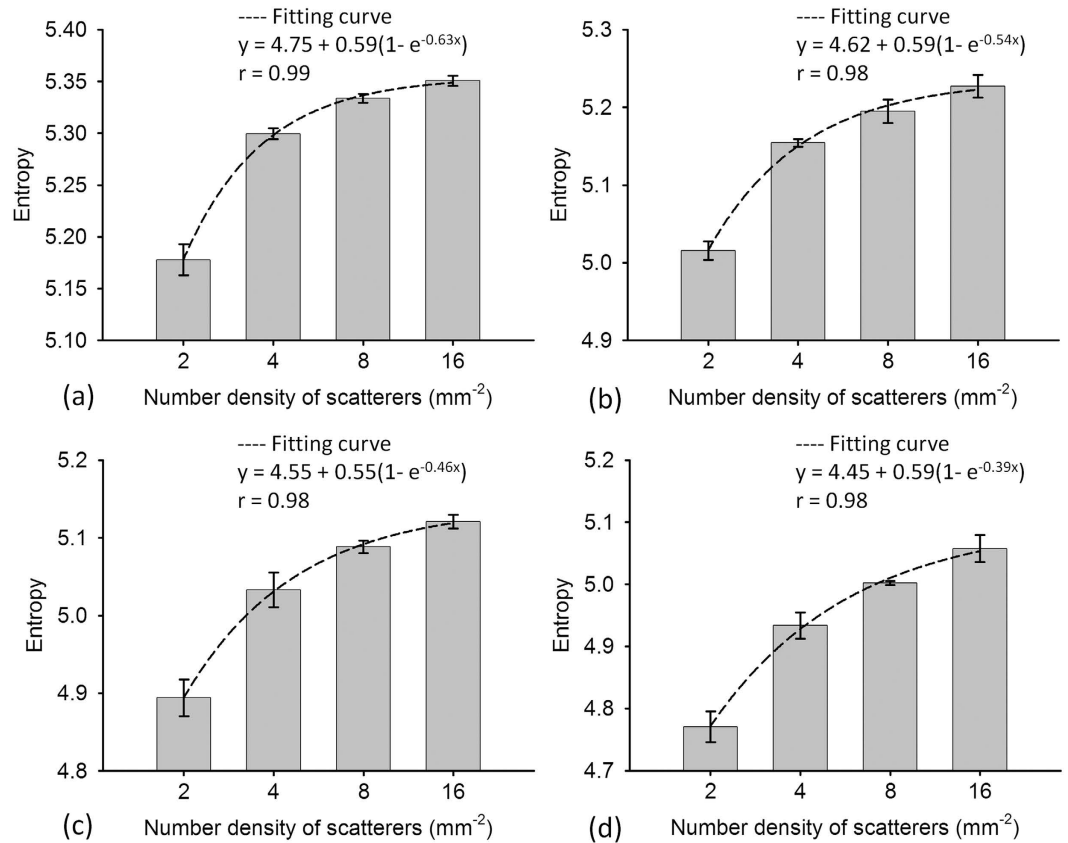


Figure 3. Simulated entropy as a function of the number density of the scatterers obtained at different SLs. (a) SL = 1; (b) SL = 2; (c) SL = 3; (d) SL = 4. Entropy images constructed using windows of different sizes can detect the variation in the number density of scatterers in a homogeneous medium. Data were expressed by mean \pm standard deviation.

is SNR-dependent below 20 dB⁴⁵. On the other hand, a significant dependence of entropy on frequency was not observed in the range of 5 to 8 MHz, but the transducer focus affects the entropy estimation (Fig. 10). This is largely due to that the degree of transducer focusing determines the size of the resolution cell, affecting the number of scatterers in the resolution cell that dominate the formation of backscattered signals and the corresponding estimations of statistical parameters^{27,30}. Note that the transducer focusing simultaneously accompanies the diffraction effect in the far-field, which makes the resolution cell contain a large number of scatterers to result in overestimations of parameters for tissues with a low number density of scatterers⁴⁶.

Clinical exploration. The patterns of a breast parenchyma, which is composed of fatty and fibroglandular tissues, have been shown to be associated with the risk of developing breast cancer⁴⁷. For healthy women, dense fibroglandular tissues are more common, and the corresponding density in a breast parenchyma decreases with age⁴⁸. Ideally, a normal breast parenchyma based on fibroglandular tissues causes a fully developed speckle pattern in the B-mode image, which corresponds to the envelope statistics of the Rayleigh distribution⁴³. Compared with normal breast tissue, benign fibroadenoma is composed of glandular tissues and local fibrous tissues or calcification⁴⁹. Local fibrosis or calcification may cause local changes in the sound speed, density, and hardness, causing scatterers in a tumor to exhibit higher variability in the scattering cross sections¹³. Invasive carcinoma is the most prevalent malignant tumor. The cancer cells may spread to other parts of the body through the lymphatic system and bloodstream. In particular, malignant tumors may have diversified structures and calcification patterns^{50–52}, such as (i) asymmetry and isolated dilated ducts⁵³, (ii) calcifications with a greater hardness and density⁵¹, (iii) calcifications with irregular sizes, shapes, and nonuniform spatial distributions (e.g., branching or clustered)⁵⁴, and (iv) stronger vascular flow and angiogenesis effects^{55,56}. The aforementioned characteristics are expected to further strengthen the degree of variance in the echogenicity of scatterers, causing the entropic values of malignant tumors to be lower than those of benign tumors.

Refer to the results in Figs 11 and 12. Small-window entropy imaging is superior to statistical parametric imaging in classifying benign and malignant breast tumors. Prior to proposal of small-window entropy imaging, statistical parametric imaging has been widely used in breast tissue characterization^{13,14,42,57,58}. However, some considerations and limitations exist when statistical parameters are used in practice. First, not every statistical distributions are applicable to characterizing breast tumors. For example, the estimation of the Nakagami parameter may be disturbed by the presence of structures in the breast⁵⁷. This is why researchers attempted to use the mixture of distributions as a more general approach to describe the backscattered statistics^{11,57,59}. Second,

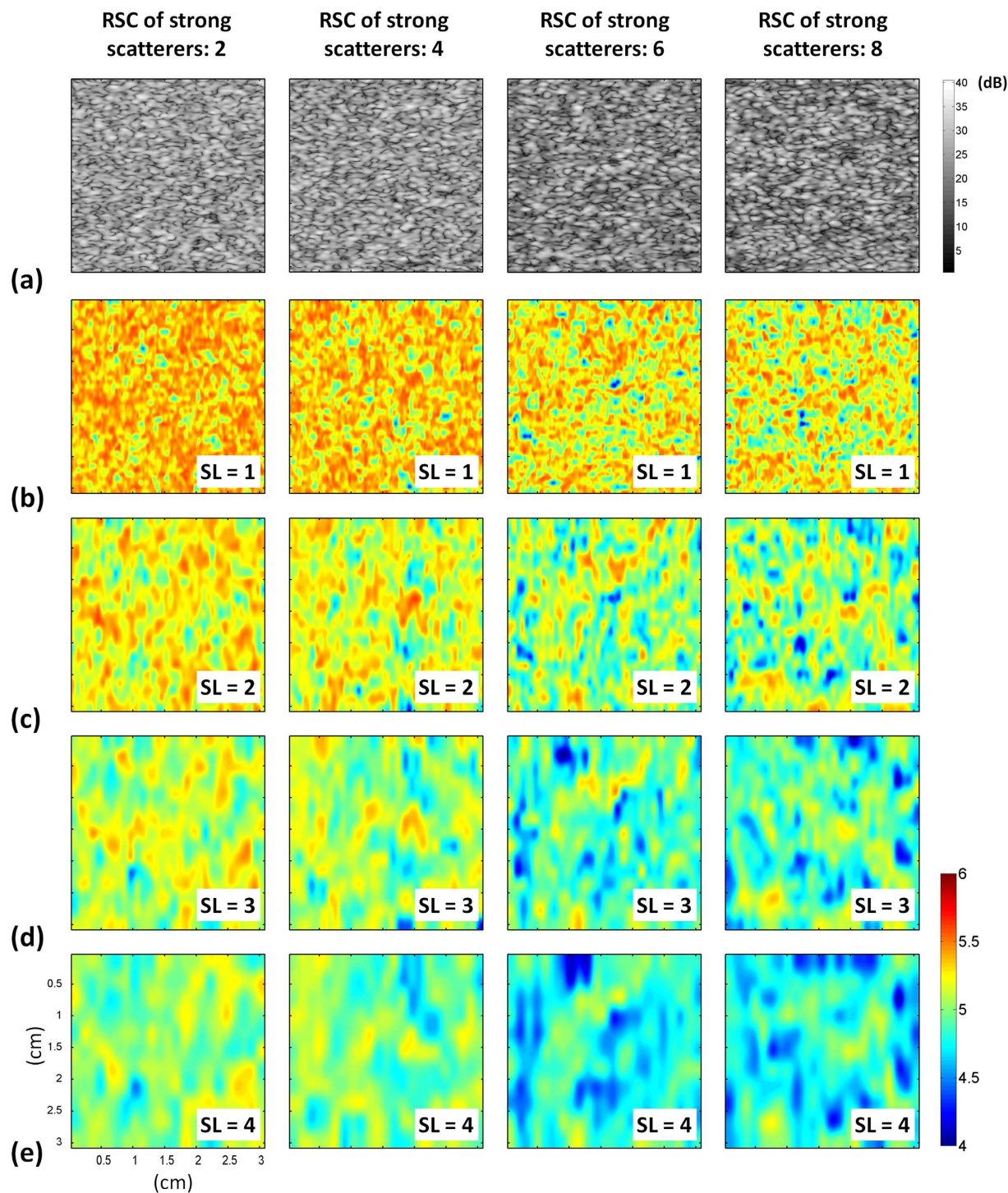


Figure 4. (a) B-mode and (b–e) entropy images of Type-II simulated phantoms containing strong scatterers with different RSCs constructed using different SLs. (b) SL = 1; (c) SL = 2; (d) SL = 3; (e) SL = 4. The dimensions for all images are the same. The grayscale and color bars represent the pixel values (the brightness) of the B-mode and entropy images, respectively. The change in the shade of the entropy images showed a decrease in the entropy because of the increasing phantom inhomogeneity.

the estimation of the statistical parameter is affected by the used estimator. Moment-based estimators are frequently used for estimating statistical parameters. Nevertheless, using a maximum likelihood estimator can yield a smaller variance in estimations⁶⁰. Although recent studies started to use different estimators for applications in tissue characterization^{31,58}, the optimal estimator for parametric imaging of breast tumors has not been concluded. Third, as mentioned in Introduction, statistical parametric imaging needs the use of a large window to

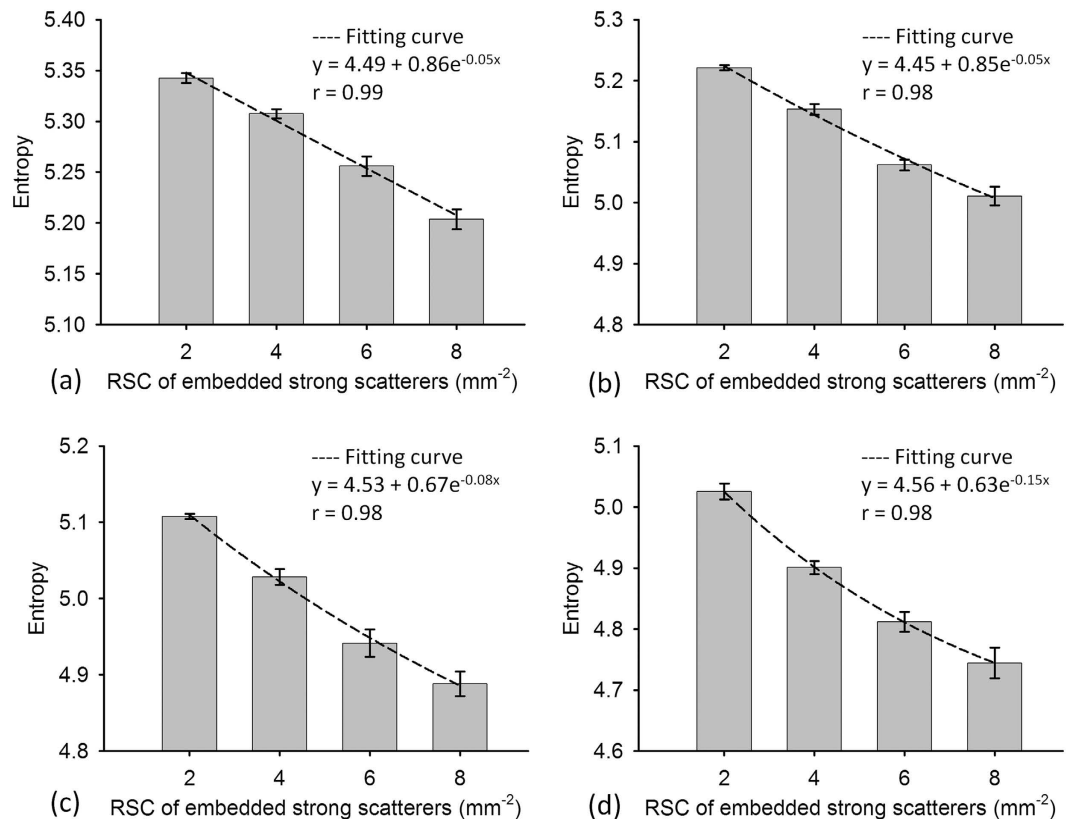


Figure 5. Simulated entropy as a function of the RSC of the embedded strong scatterers when different SLs were used. (a) SL = 1; (b) SL = 2; (c) SL = 3; (d) SL = 4. As the RSC of the strong scatterers increased, entropy in the image decreased. Data were expressed by mean \pm standard deviation.

capture sufficient data points for stable parameter estimations. A significant boundary artifact will occur in the parametric image to degrade the performance in classifying breast tumors¹³.

Compared with statistical parameters, entropy enables using a small window for implementing ultrasound parametric imaging. In this condition, boundary artifacts can be largely suppressed to improve the classification of breast tumors (Fig. 12), as discussed below.

Suppression of boundary artifacts. Boundary artifacts frequently appear at the interfaces of tissues in ultrasound parametric imaging¹³ because the existence of edges and boundaries affects the backscattered statistics^{57,59}. When a sliding window moves across the interface during parametric imaging, the window covers not only the backscattered data from the interface but also those from the background tissues. The difference in the echo amplitude of the interface and background tends to narrow the probability distribution of the data, causing the parameter to be underestimated and generating a boundary artifact. Among all possibilities, using a small window for parametric imaging is the simplest approach to suppress the boundary artifacts. Information entropy is a relative measure of the signal uncertainty, not a model-based parameter or an absolute physical estimate. Therefore, unlike the distribution parameters, entropy allows calculation using less data points acquired from a small window as long as its detectability in the properties of scatterers can be obtained. This study demonstrated that entropy combined with the small-window technique can implement parametric imaging to characterize tissues without significant boundary artifacts (Figs 6 and 11).

Conclusions

Computer simulations and phantom experiments were conducted to investigate ultrasound small-window entropy imaging and its performance in detecting changes in the properties of scatterers. Small-window entropy imaging constructed using SL = 1 effectively visualizes changes in the number density of scatterers and inhomogeneity without significant boundary artifacts. Clinical measurements on breast tumors also showed the usefulness of small-window entropy imaging in practical tissue characterization. Information entropy enables using a small window for implementing high-resolution ultrasound parametric imaging.

Materials and Methods

Simulations. Two-dimensional (2D) computer simulations were executed at a sampling rate of 50 MHz and a sound speed of 1540 m/s to generate image RF data; previous studies have detailed the simulation method^{31,43,61}. A 5-MHz Gaussian pulse (a pulse length of 0.89 mm, a bandwidth of 80%, and a beam width of

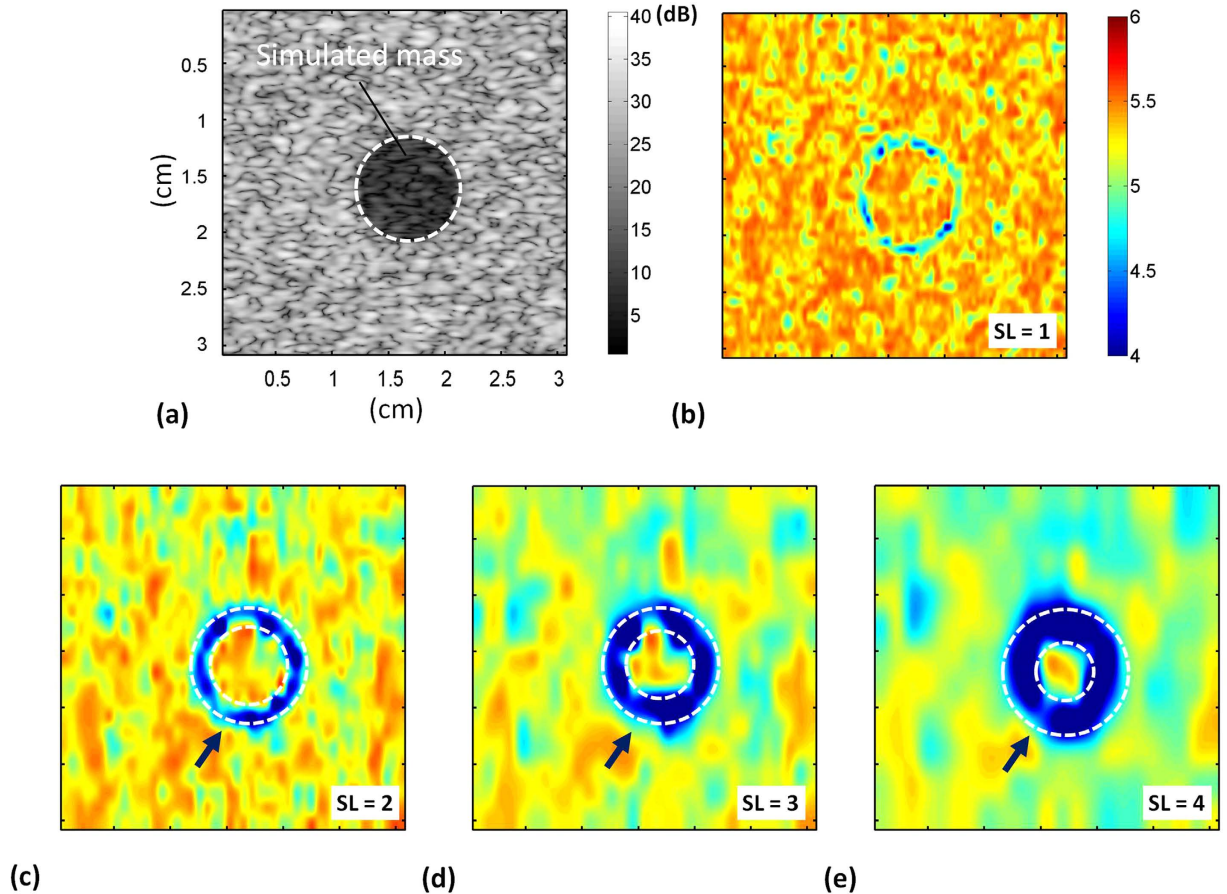


Figure 6. (a) B-mode and (b–e) entropy images of a simulated mass obtained using windows of different sizes. (b) SL = 1; (c) SL = 2; (d) SL = 3; (e) SL = 4. The dimensions for all images are the same. The grayscale and color bars represent the pixel values (the brightness) of the B-mode and entropy images, respectively. The boundary artifact was conspicuous when windows with a large SL were used, and it gradually diminished as the SL decreased from 4 to 1.

1.66 mm) was generated as the incident wave with a 2D resolution cell with an area of approximately 1.48 mm² (0.89 mm × 1.66 mm). The computer phantom Z is a 2D matrix with randomly positioned delta functions that describe the spatial arrangement of K scatterers; it is given by

$$Z(x, y) = \sum_{n=1}^K \delta(x - x_n, y - y_n). \quad (1)$$

Simulated image RF data were obtained by convoluting the incident wave with the computer phantoms.

A total of five phantoms with sizes 3 cm × 3 cm were constructed for each number density of scatterers (2, 4, 8, and 16 scatterers/mm²). A computer phantom with 16 scatterers/mm² has approximately 24 scatterers per resolution cell (>10 scatterers per resolution cell), which is sufficient to produce the fully-developed speckle B-mode image (the backscattered statistics follow Rayleigh distribution)³⁰. In this study, we term these phantoms Type-I phantoms to simulate changes in the backscattered statistics from pre-Rayleigh to Rayleigh distributions. The magnitude of the delta function is 1 and is considered the relative RSC for each scatterer in the phantom.

To simulate an inhomogeneous medium with different degrees of scatterer echogenicity variance, we added randomly distributed strong scatterers at a number density of 1 scatterer/mm² in each Type-I phantom; these Type-I phantoms containing strong scatterers are defined as Type-II phantoms. The RSCs of the strong scatterers were adjusted by multiplying weight factors and the delta functions. Thus, Type-II phantoms Z_s are expressed as

$$Z_s(x, y) = \sum_{n=1}^K \delta(x - x_n, y - y_n) + \sum_{n=1}^M c \cdot \delta(x - x_n, y - y_n), \quad (2)$$

where c (=2, 4, 6, and 8) is the weight factor used to simulate the RSCs of strong scatterers, and M represents the number of strong scatterers. For each weight factor, five Type-II phantoms were produced for signal formation and analysis. Adjusting the RSC was not used for simulating the properties of real tissues. This is a method used to generate ultrasound signals with changes in the backscattered statistics from Rayleigh to pre-Rayleigh distributions, as proposed in our previous study³¹. Based on the suggestion given in a previous study³⁰, strong scatterers

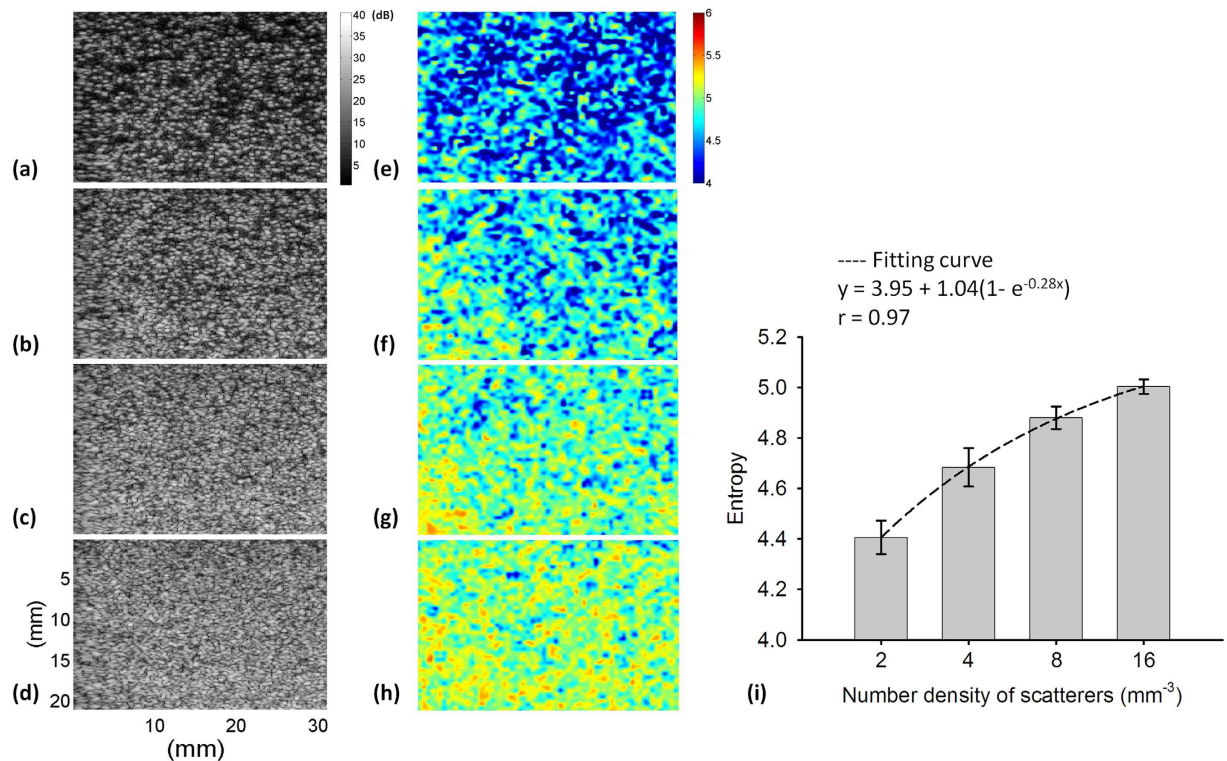


Figure 7. (a–d) B-mode images of Type-A agar phantoms with number densities of scatterers of 2, 4, 8, and 16 scatterers/mm³ (SL = 1; frequency = 6 MHz; scanned at a focus of 1 cm). The dimensions for all images are the same. The grayscale and color bars represent the pixel values (the brightness) of the B-mode and entropy images, respectively. (e–h) Entropy images corresponding to (a–d). (i) Entropy as a function of the number density of scatterers. Data were expressed by mean \pm standard deviation.

contribute amplitude values 4 times the mean amplitude of random scatterers. Therefore, the range of the weight factor c from 2 to 8 was chosen to simulate variations in the RSCs of strong scatterers.

The existence of edges and boundaries in B-scan images alters the statistics of the backscattered echo⁵⁹. Therefore, we created Type-III phantoms, each containing a background material and an embedded cylindrical object with a diameter of 1 cm. Both the background and the cylindrical object have the same number density of scatterers (16 scatterers/mm²). The RSCs of the scatterers in the background and the cylindrical object were set to 1 and 0.1, respectively. The Type-III phantoms were generated to simulate the mass to explore the boundary artifact of the entropy image corresponding to the interface between the tissue background and the target.

Note that the effects of frequency, diffraction due to transducer focusing, and attenuation were not considered in the simulation model. To explore performances of ultrasound entropy imaging in scatterer characterization under frequency, diffraction, and attenuation effects, phantom experiments were further conducted.

Phantom experiments. The phantoms were constructed by boiling and cooling agar–water mixtures (dissolving 3 g of the agar powder into 200 mL of water) and adding different materials, including glass beads with diameters of 75 μ m (Model 59200U, Supelco, Bellefonte, PA, USA), graphite powder with diameters < 20 μ m (Model 282863, Sigma-Aldrich, St. Louis, MO, USA), and soybean-oil lipid emulsions (Intrafat, Nihon Pharmaceutical Industry, Osaka, Japan). Both the glass beads and graphite powder were used as acoustic scatterers in the scattering medium, and the materials of the lipid emulsions were used to produce an acoustic attenuation effect in the phantoms⁶². Three types of phantoms were constructed, namely Type-A, Type-B, and Type-C. A tissue-mimicking breast phantom (Model BPB170, Blue Phantom, Redmond, WA, USA) was used as a Type-D phantom to provide a simulated mass.

The properties and materials of each type of phantom are shown in Table 1. For Type-A phantoms, the number densities of scatterers (NDS) were determined by

$$\text{NDS} = \frac{M}{\frac{4}{3}\pi r_g^3 \cdot \rho \cdot V}, \quad (3)$$

where M , r_g , and ρ correspond to the mass, radius, and density of the glass beads, respectively, and V denotes the volume of the agar phantom. The number densities of scatterers for Type-A phantoms were set the same as those in the simulations (2 to 16 scatterers/mm³). For Type-B and C phantoms, a large amount of graphite powder is required to be added for the formation of significant backscattered signals because graphite powders with small diameters (< 20 μ m) are relatively weak scatterers. Thus, the same number densities of scatterers are not applicable

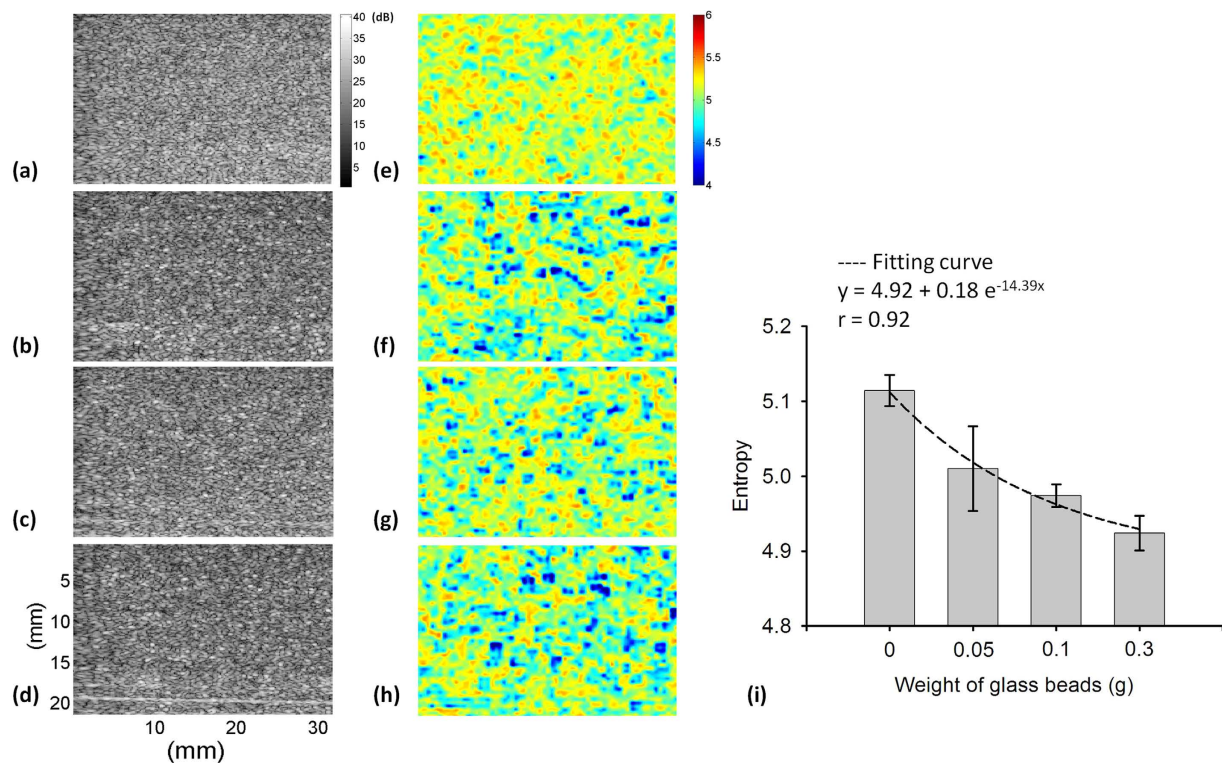


Figure 8. (a–d) B-mode images of Type-B agar phantoms to which 0, 0.05, 0.1, and 0.3 g of glass beads were added (SL = 1; frequency = 6 MHz; scanned at a focus of 1 cm). The dimensions for all images are the same. The grayscale and color bars represent the pixel values (the brightness) of the B-mode and entropy images, respectively. (e–h) Entropy images corresponding to (a–d). (i) Entropy as a function of the weight of glass beads. Data were expressed by mean \pm standard deviation.

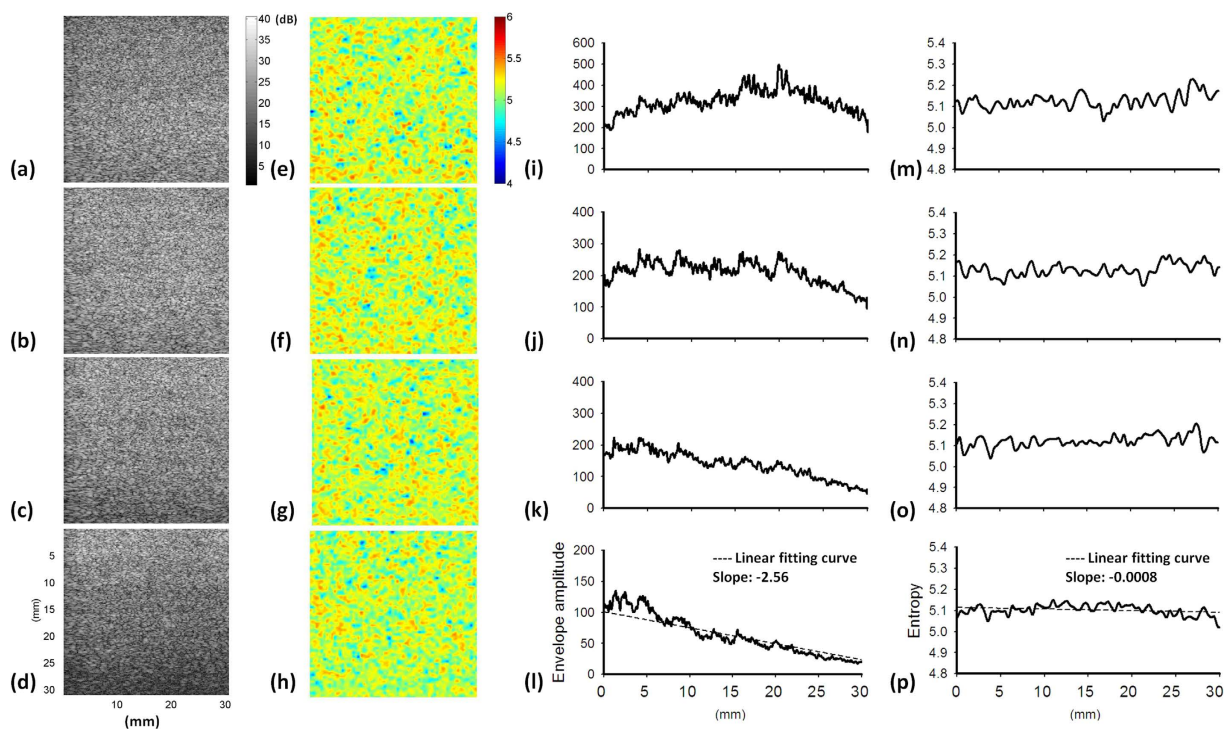


Figure 9. (a–d) B-mode images of Type-C agar phantoms to which lipid emulsions of 0%, 5%, 10%, and 20% were added (SL = 1; frequency = 6 MHz; scanned at a focus of 1 cm). The dimensions for all images are the same. The grayscale and color bars represent the pixel values (the brightness) of the B-mode and entropy images, respectively. (e–h) Entropy images corresponding to (a–d). (i) Entropy as a function of lipid concentration.

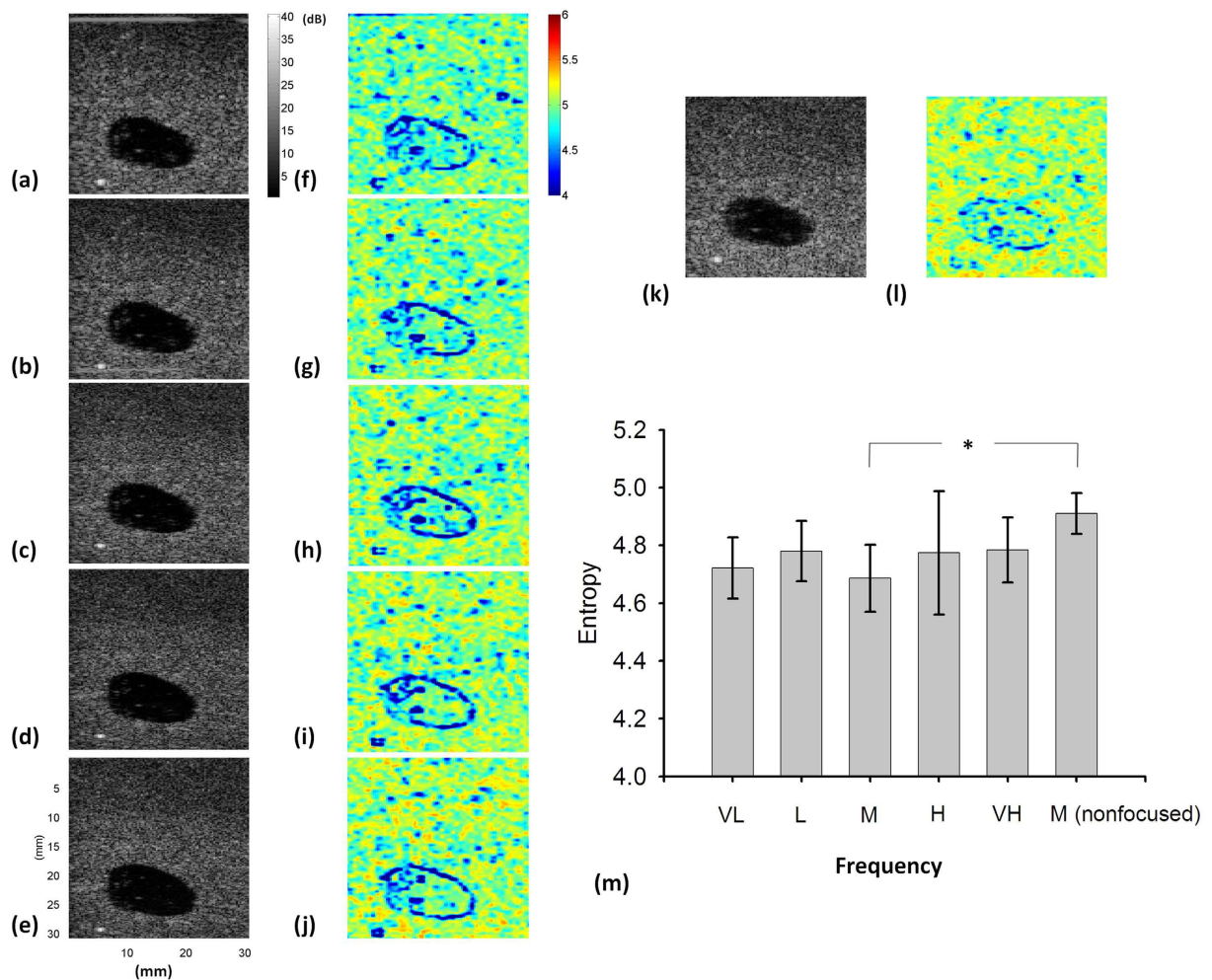


Figure 10. (a–e) B-mode images of the Type-D breast phantom with a mass at frequencies of 5, 5.5, 6, 7.5, and 8 MHz (SL = 1; scanned at a focus of 2 cm). (f–j) Entropy images corresponding to (a–e). (k–l) B-mode and entropy images scanned using 6 MHz and a focal length of 3 cm. The dimensions for all images are the same. The grayscale and color bars represent the pixel values (the brightness) of the B-mode and entropy images, respectively. (m) Entropy of the mass as a function of different settings (the “*” symbol indicates a p value < 0.05). Data were expressed by mean \pm standard deviation.

in Type-B and C phantoms. Alternatively, the scatterer concentration (the ratio of powder weight to the volume of the phantom) was used. Using equation (3) and assuming that the diameter of graphite powder is $20\ \mu\text{m}$, the number density of scatterers in the background of the phantom (made using 2 g graphite powder and 200 mL water) is estimated to be at least $1000\ \text{scatterers}/\text{mm}^3$. This estimated number density ensures that a large number of randomly distributed scatterers exist in the resolution cell, making backscattered envelopes obey the Rayleigh distribution.

Five independent scans of each phantom were performed using a commercial ultrasound imaging system (Model 3000, Terason, Burlington, MA, USA) with a linear array transducer (Model 10L5, Terason). The Terason scanner enables RF data access and frequency selection. The transmitting central frequency can be set at approximately 5, 5.5, 6, 7.5, and 8 MHz (denoted by VL, L, M, H, and VH, respectively) by using the software, and the pulse-echo tests of the transducer in the laboratory showed that the pulse length of the transducer was approximately three times the wavelength. In the experiments on the Type-A, -B, and -C phantoms, the image RF data consisted of 128 A-lines of backscattered signals, which were acquired using the same transmitting frequency (6 MHz) and a focus of 1 cm to investigate the dependency of entropy on the number density of scatterers, the degree of variance in the echogenicity, and the attenuation effect. In the experiments on the Type-D phantom, different transmitting frequencies and focus settings were used to explore the effects of frequency and focus on ultrasound entropy imaging.

Clinical measurements. Clinical data were collected for preliminarily validating ultrasound entropy imaging for characterizing tissues. This study was approved by the Institutional Review Board of National Taiwan University Hospital, and signed informed consent forms were obtained from the patients. All the experimental methods were carried out in accordance with the approved guidelines. At the Department of Surgery, female

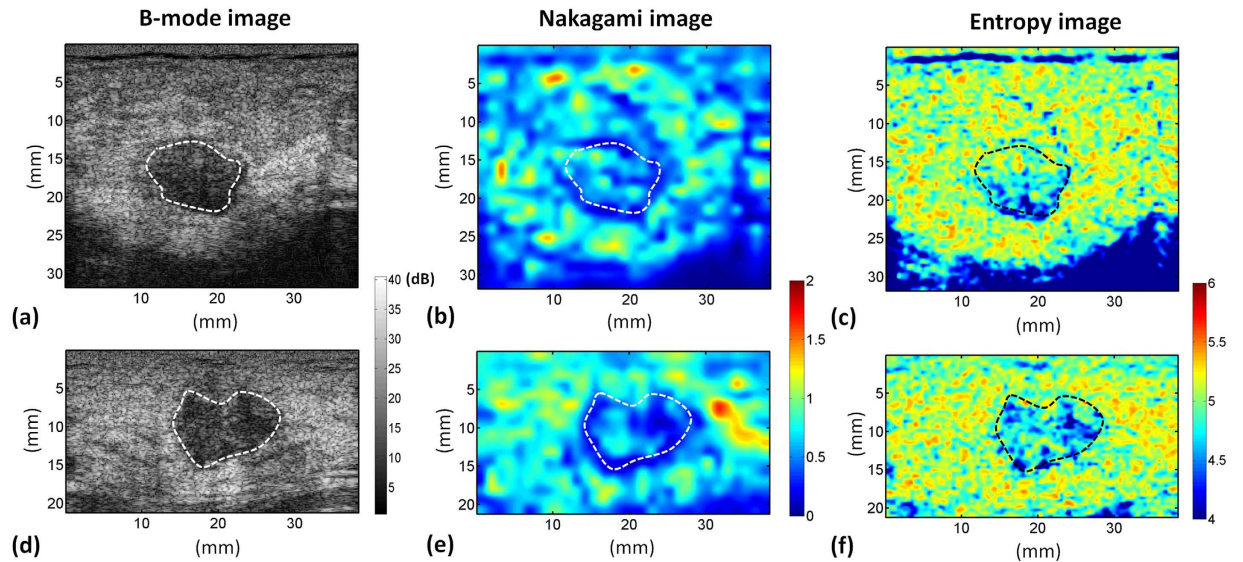


Figure 11. B-mode, Nakagami, and entropy (SL = 1) images of benign (a–c) and malignant (d–f) breast tumors. The shade of the Nakagami and entropy images of the malignant tumor was darker than that of the benign tumor.

patients that required clinical biopsy examinations of masses were recruited. Breast tumors were classified as benign or malignant by a pathologist according to the biopsy reports. Prior to the biopsy examination, ultrasound scanning of the patients was performed by the same sonographer to reduce the inter-rater variability of ultrasound scan. For each patient, five scans were performed to collect grayscale B-mode images and the corresponding RF backscattered data using the same Terason system and linear array transducer for manual tumor contour segmentation and entropy imaging, respectively. Images of tumors with incomplete contours caused by posterior shadow effect were excluded in the analysis. Under the above criterion, a total of 63 patients ($n = 63$) were recruited, including 33 benign (fibroadenoma) and 30 malignant (invasive carcinoma) masses.

Entropy estimation. Shannon proposed the information entropy to quantify information^{32,63}. In ultrasound imaging, the Shannon entropy of backscattered RF signals $f(t)$ is defined as the negative of the logarithm of the backscattered probability distribution $w(y)$ ³⁴:

$$H_C \equiv - \int_{y_{\min}}^{y_{\max}} w(y) \log_2[w(y)] dy, \quad (4)$$

where y_{\min} and y_{\max} represent the minimal and maximal values of $f(t)$, respectively. In this study, the statistical histogram of RF signals was used to represent $w(y)$ ^{28,40}. Practically, Shannon entropy is obtained as a discrete form of equation (4) using the digitized versions of the underlying continuous waveform. Entropy is a measure of the uncertainty or unpredictability of ultrasound backscattered signals.

Algorithmic scheme of entropy imaging. Figure 13 shows the algorithmic scheme designed for constructing the B-mode and information entropy images using the backscattered signals. The algorithm was programmed using MATLAB software (version R2012a, The MathWorks, Inc., MA, USA). The envelope image was constructed using the absolute value of the Hilbert transform to demodulate each scan line, and the B-mode image was formed using a logarithm-compressed envelope image at a dynamic range of 40 dB.

Concurrently, the beamformed RF data were used for entropy estimation and imaging using a standard sliding window algorithm, and the entropic parametric map was constructed through the following two steps: (i) a square window within the image data was used to acquire local RF signals for establishing the probability density function $w(y)$ and calculating the entropy value using equation (4), which was assigned as the new pixel located in the center of the window; and (ii) the window was moved across the entire range of image data in steps of the number of pixels corresponding to a window overlap ratio, and step 1 was repeated to yield the entropy parametric map. A low window overlap ratio results in a low line density of a parametric image. The decreased line density decreases the spatial resolution of an image⁶⁴, making spatial information insufficient to describe the region of interest (ROI). A high window overlap ratio results in a high line density. However, the computational efficiency and speed may reduce because a large amount of data must be processed. A recent study showed that the window overlap ratio does not affect ultrasound parametric imaging and estimations of statistical parameters⁶¹. To have a trade-off between the image resolution and the computational time, a 50% window overlap ratio was used.

Data analyses for simulation. To explore the effect of the window size on the entropy image, the entropic parametric map corresponding to each image data was constructed using square sliding windows with SLs

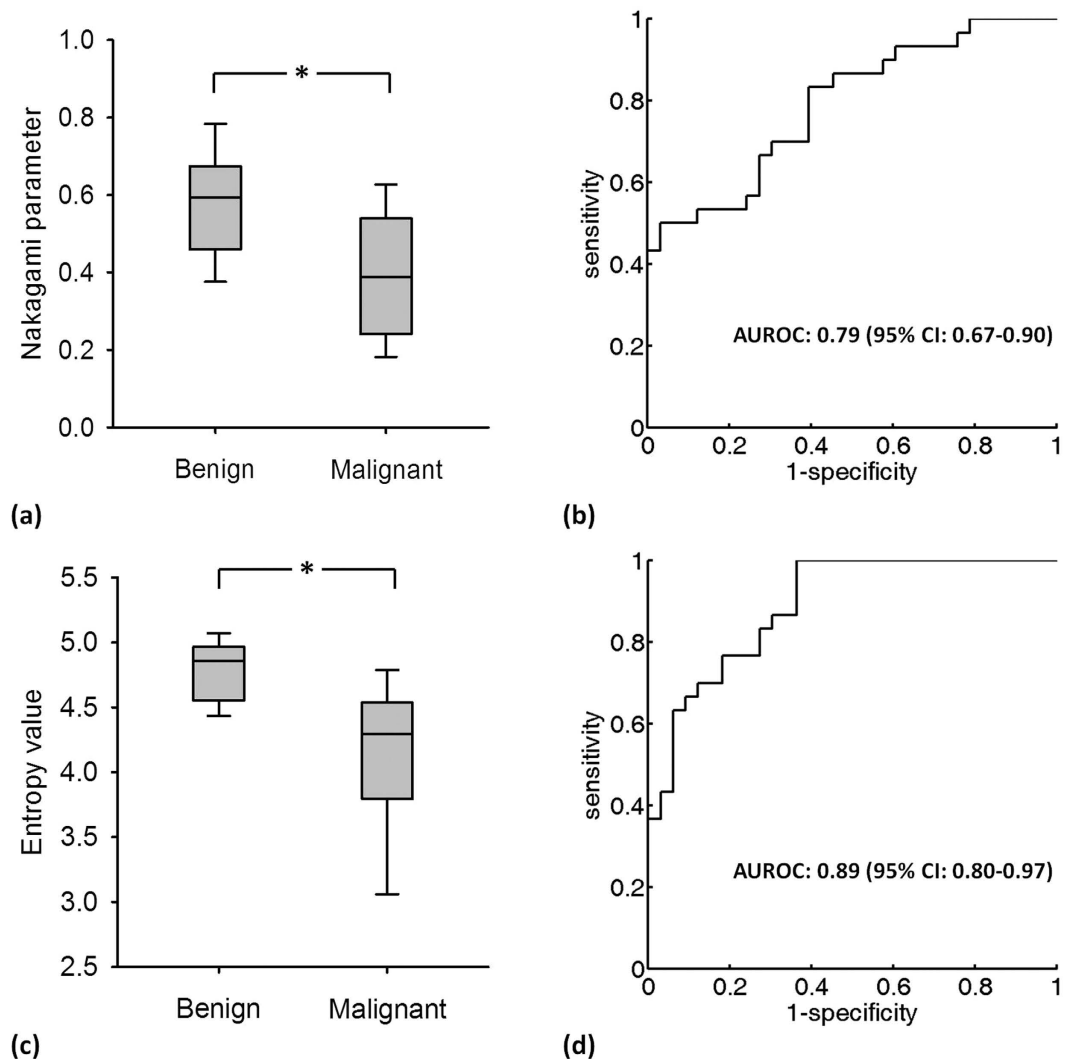


Figure 12. (a) The median Nakagami parameters for benign and malignant tumors were 0.59 (IQR: 0.46–0.67) and 0.46 (IQR: 0.28–0.55), respectively ($p < 0.05$). (b) ROC curve for using the Nakagami image to classify benign and malignant tumors. The AUROC was 0.75. (c) The median entropies for benign and malignant tumors were 4.86 (IQR: 4.57–4.96) and 4.37 (IQR: 4.01–4.61), respectively (the “*” symbol indicates a p value < 0.05). (d) ROC curve for using the entropy image to classify benign and malignant tumors. The AUROC was 0.82.

ranging from 1 to 4 times the transducer pulse length (denoted as $SL = 1, 2, 3,$ and 4). For each simulated entropy image, the pixel data were acquired from an ROI with a size of $5 \times 5 \text{ mm}^2$ to explore the entropy value as a function of the SL, number density of the scatterers, and RSC of the embedded strong scatterers. The trends of data were described by curve fitting, and data were expressed by mean \pm standard deviation.

Data analyses for phantom experiments. $SL = 1$ was used for entropy imaging of phantom data according to the findings in the simulations (please see the section of Results). ROIs ($5 \times 5 \text{ mm}^2$) located in the focal zone were applied to the phantom results to investigate the effects of scatterer properties, attenuation, frequency, and focus on entropy values. Data were expressed by mean \pm standard deviation. To evaluate statistical significance, an independent t test was performed to calculate the probability value p .

Data analyses for clinical data. The entropy images ($SL = 1$) of breast tumors were analyzed according to the ROIs that were manually determined by the surgeon, who was blind to the biopsy reports. To compare the performance of entropy imaging with that of statistical parametric imaging in clinical breast tumor characterization, Nakagami images of each patient were also constructed and the same ROIs determined by the surgeon were applied to the Nakagami images for analysis. The algorithm of Nakagami imaging was based on the sliding window processing, which was the same technique as that described in Fig. 13. The envelope image was obtained from the absolute value of the Hilbert Transform of the RF data. A Nakagami image was constructed using a

Methodology		Small-window ultrasound entropy imaging	Nakagami statistical parametric imaging
Median (IQR) of the Nakagami parameter	Benign	4.86 (4.57–4.96)	0.59 (0.46–0.67)
	Malignant	4.29 (3.87–4.51)	0.38 (0.25–0.53)
Dynamic range of the parameter		1.73–5.09	0.24–0.87
Cutoff value		4.52	0.47
Sensitivity%		76.66%	70.00%
Specificity%		81.81%	69.69%
Accuracy%		79.36%	69.84%
LR+		4.21	2.31
LR–		0.28	0.43
PPV%		79.31	67.74
NPV%		79.41	71.87
AUROC (95% CI)		0.89 (0.80–0.97)	0.79 (0.67–0.90)

Table 2. Performance comparisons between ultrasound small-window entropy and Nakagami imaging in classifying benign and malignant breast tumors. LR+: positive likelihood ratio, LR–: negative likelihood ratio, PPV: positive predictive value, NPV: negative predictive value, AUROC: area under the receiver operating characteristics curve.

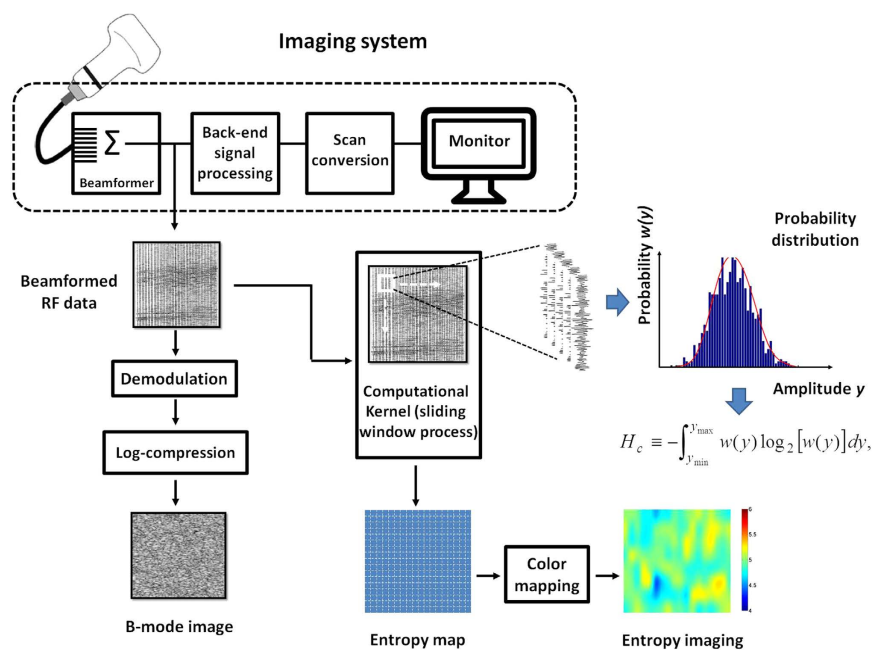


Figure 13. The algorithmic scheme designed for constructing the B-mode and information entropy images using the backscattered signals. The B-mode image was formed using a logarithm-compressed envelope image. The image RF data were used for entropy estimation and imaging using a standard sliding window algorithm.

square window (SL = 3; a 50% window overlap ratio) sliding on the envelope image for collecting local envelope data R and estimating local Nakagami parameters m by

$$m = \frac{[E(R^2)]^2}{E[R^2 - E(R^2)]^2}, \quad (5)$$

SL = 3 was used because the side length of the window corresponding to three times the pulse length of the transducer enables a stable estimation of the Nakagami parameter^{13,15,25,29}. The Nakagami parameters and the entropy values of benign and malignant tumors were shown in the box plots (expressed by the median and interquartile range, IQR) for comparisons. For evaluating statistical significance, an independent t test was performed to calculate the p value. The ROC curve was used to evaluate the clinical performances of the Nakagami and entropy images in classifying benign and malignant tumors. Statistical analysis was performed using SigmaPlot (version 9.0, Systat Software, Inc., CA, USA).

References

- Gill, I. S. & Ukimura, O. Contemporary interventional ultrasonography in urology. Springer Science & Business Media, Berlin (page 153) (2009).
- Burckhardt, C. B. Speckle in ultrasound B-mode scans. *IEEE Trans. Sonics Ultrason.* **SU-25**, 1–6 (1978).
- Wagner, R. F., Insana, M. F. & Brown, D. G. Statistical properties of radio-frequency and envelope detected signals with applications to medical ultrasound. *J. Opt. Soc. Am.* **4**, 910–922 (1987).
- Weng, L., Reid, J. M., Shankar, P. M. & Soetanto, K. Ultrasound speckle analysis based on the K distribution. *J. Acoust. Soc. Am.* **89**, 2992–2995 (1991).
- Dutt, V. & Greenleaf, J. F. Ultrasound echo envelope analysis using a homodyned K distribution signal model. *Ultrason. Imaging* **16**, 265–287 (1994).
- Shankar, P. M. A model for ultrasonic scattering from tissues based on K-distribution. *Phys. in Med. and Biol.* **40**, 1633–1649 (1995).
- Shankar, P. M. A general statistical model for ultrasonic backscattering from tissues. *IEEE Trans. Ultrason. Ferroelec. Freq. Contr.* **47**, 727–736 (2000).
- Shankar, P. M. A compounding scattering pdf for the ultrasonic echo envelope and its relationship to K and Nakagami distributions. *IEEE Trans. Ultrason. Ferroelec. Freq. Contr.* **50**, 339–343 (2003).
- Karmeshu & Agrawal, R. Study of ultrasonic echo envelope based on Nakagami-inverse Gaussian distribution. *Ultrasound Med. Biol.* **32**, 371–376 (2006).
- Agrawal, R. & Karmeshu Ultrasonic backscattering in tissue: characterization through Nakagami-generalized inverse Gaussian distribution. *Comput. Biol. Med.* **37**, 166–172 (2006).
- Shankar, P. M. A statistical model for the ultrasonic backscattered echo from tissue containing microcalcifications. *IEEE Trans. Ultrason. Ferroelec. Freq. Contr.* **60**, 932–942 (2013).
- Mamou, J. & Oelze, M. L. *Quantitative ultrasound in soft tissues*. Springer, New York, (2013).
- Tsui, P. H. *et al.* Ultrasonic Nakagami imaging: a strategy to visualize the scatterer properties of benign and malignant breast tumors. *Ultrasound Med. Biol.* **36**, 209–217 (2010).
- Liao, Y. Y. *et al.* Strain-compounding technique with ultrasound Nakagami imaging for distinguishing between benign and malignant breast tumors. *Med. Phys.* **39**, 2325–2333 (2012).
- Ho, M. C. *et al.* Relationship between ultrasound backscattered statistics and the concentration of fatty droplets in livers: an animal study. *PLoS One* **8**, e63543 (2013).
- Ho, M. C. *et al.* Early detection of liver fibrosis in rats using 3-D ultrasound Nakagami imaging: a feasibility evaluation. *Ultrasound Med. Biol.* **40**, 2272–2284 (2014).
- Yang, X. *et al.* Quantitative ultrasonic Nakagami imaging of neck fibrosis after head and neck radiation therapy. *Int J Radiat Oncol Biol Phys* **92**, 407–414 (2015).
- Caixinha, M., Jesus, D. A., Velte, E., Santos, M. J. & Santos, J. B., Using ultrasound backscattering signals and Nakagami statistical distribution to assess regional cataract hardness. *IEEE Trans Biomed Eng.* **61**, 2921–2929 (2014).
- Lin, Y. H., Huang, C. C. & Wang, S. H. Quantitative assessments of burn degree by high-frequency ultrasonic backscattering and statistical model. *Phys. in Med. and Biol.* **56**, 757–773 (2010).
- Gu, X., Wei, M., Zong, Y., Jiang, H. & Wan, M. Flow quantification with nakagami parametric imaging for suppressing contrast microbubbles attenuation. *Ultrasound Med. Biol.* **39**, 660–669 (2013).
- Zhou, Z. *et al.* Monitoring radiofrequency ablation using real-time ultrasound Nakagami imaging combined with frequency and temporal compounding techniques. *PLoS One* **10**, e0118030 (2015).
- Yu, X. & Lee, W. N. Characterization of the heart muscle anisotropy using ultrasound Nakagami imaging. *IEEE Ultrason. Symp. Proc.* **1**, 2367–2370 (2014).
- Valckx, F. M., Thijsse, J. M., Geemen, A. J. v., Rotteveel, J. J. & Mullaart, R. Calibrated parametric medical ultrasound imaging. *Ultrason. Imaging* **22**, 57–72 (2000).
- Davignon, F., Deprez, J. F. & Basset, O. A parametric imaging approach for the segmentation of ultrasound data. *Ultrasonics* **43**, 789–801 (2005).
- Tsui, P. H. & Chang, C. C. Imaging local scatterer concentrations by the Nakagami statistical model. *Ultrasound Med. Biol.* **33**, 608–619 (2007).
- Li, M. L., Li, D. W., Liu, H. L. & Lin, M. S. Ultrasonic Nakagami visualization of HIFU-induced thermal lesions. *IEEE Ultrason. Symp. Proc.* 2251–2253 (2010).
- Yu, X., Guo, Y., Huang, S. M., Li, M. L. & Lee, W. N. Beamforming effects on generalized Nakagami imaging. *Phys Med Biol* **60**, 7513–7531 (2015).
- Smolikova, R., Wachowiak, M. P. & Zurada, J. M. An information-theoretic approach to estimating ultrasound backscatter characteristics. *Comput Biol Med* **34**, 355–370 (2004).
- Tsui, P. H., Huang, C. C., Sun, L., Dailey, S. H. & Shung, K. K. Characterization of lamina propria and vocal muscle in human vocal fold tissue by ultrasound Nakagami imaging. *Med. Phys.* **38**, 2019–2026 (2011).
- Tuthill, T. A., Sperry, R. H. & Parker, K. J. Deviations from Rayleigh statistics in ultrasonic speckle. *Ultrason. Imaging* **10**, 81–89 (1988).
- Tsui, P. H., Wan, Y. L., Tai, D. I. & Shu, Y. C. Effects of estimators on ultrasound Nakagami imaging in visualizing the change in the backscattered statistics from a Rayleigh distribution to a pre-Rayleigh distribution. *Ultrasound Med. Biol.* **41**, 2240–2251 (2015).
- Shannon, C. E. A Mathematical Theory of Communication. *Bell System Technical Journal* **27**, 379–423 (1948).
- Hughes, M. S. Analysis of ultrasonic waveforms using Shannon entropy. *IEEE Ultrason. Symp. Proc.* **1**, 1205–1209 (1992).
- Hughes, M. S. Analysis of digitized waveforms using Shannon entropy. *J. Acoust. Soc. Am.* **93**, 892–906 (1993).
- Hughes, M. S. *et al.* Properties of an entropy-based signal receiver with an application to ultrasonic molecular imaging. *J. Acoust. Soc. Am.* **121**, 3542–3557 (2007).
- Hughes, M. S., McCarthy, J. E., Marsh, J. N. & Wickline, S. A. Joint entropy of continuously differentiable ultrasonic waveforms. *J. Acoust. Soc. Am.* **133**, 283–300 (2013).
- Hughes, M. S. *et al.* Characterization of digital waveforms using thermodynamic analogs: detection of contrast-targeted tissue *in vivo*. *IEEE Trans. Ultrason. Ferroelec. Freq. Contr.* **53**, 1609–1616 (2006).
- Hughes, M. S. *et al.* Properties of an entropy-based signal receiver with an application to ultrasonic molecular imaging. *J. Acoust. Soc. Am.* **121**, 3542–3557 (2007).
- Wallace, K. D. *et al.* Sensitive ultrasonic delineation of steroid treatment in living dystrophic mice with energy-based and entropy-based radio frequency signal processing. *IEEE Trans. Ultrason. Ferroelec. Freq. Contr.* **54**, 2291–2299 (2007).
- Zhou, Z. *et al.* Entropic imaging of cataract lens: an *in vitro* study. *PLoS One* **9**, e96195 (2014).
- Yamada, H. *et al.* A pilot approach for quantitative assessment of liver fibrosis using ultrasound: preliminary results in 79 cases. *J. Hepatol.* **44**, 68–75 (2006).
- Shankar, P. M. Use of non-Rayleigh statistics for the identification of tumors in ultrasonic B-scans of the breast. *IEEE Trans. Ultrason. Ferroelec. Freq. Contr.* **12**, 687–692 (1993).
- Tsui, P. H. Ultrasound detection of scatterer concentration by weighted entropy. *Entropy* **17**, 6598–6616 (2015).
- Byra, M., Nowicki, A., Piotrkowska-Wroblewska, H., Litniewski, J. & Dobruch-Sobczak, K. Correcting the influence of tissue attenuation on Nakagami distribution shape parameter estimation. *IEEE Ultrason. Symp. Proc.* **1**, 1–4 (2015).

45. Tsui, P. H., Wang, S. H., Huang, C. C. & Chiu, C. Y. Quantitative analysis of noise influence on the detection of scatterer concentration by Nakagami parameter. *J. Med. Biol. Eng.* **25**, 45–51 (2005).
46. Tsui, P. H. & Wang, S. H. The effect of transducer characteristics on the estimation of Nakagami parameter as a function of scatterer concentration. *Ultrasound Med. Biol.* **30**, 1345–1353 (2004).
47. Nie, K. *et al.* Quantitative analysis of breast parenchymal patterns using 3D fibroglandular tissues segmented based on MRI. *Med Phys* **37**, 217–226 (2010).
48. Chen, J. H., Yu, H., Lin, M., Mehta, R. S. & Su, M. Y. Background parenchymal enhancement in the contralateral normal breast of patients undergoing neoadjuvant chemotherapy measured by DCE-MRI. *Magn Reson Imaging* **31**, 1465–1471 (2013).
49. Cotran, R. S., Kumar, V. & Collins, T. *Robbins pathologic basis of disease*. W.B. Saunders Company, San Diego, 1998).
50. Busing, C. M., Keppler, U. & Menges, V. Differences in microcalcification in breast tumors. *Virchows Arch.* **393**, 307–313 (1981).
51. Olson, S. L. *et al.* Breast calcifications: analysis of imaging properties. *Radiology* **169**, 329–332 (1988).
52. Shen, L., Rangayyan, R. M. & Desautels, J. L. Application of shape analysis to mammographic calcifications. *IEEE Trans. Med. Imaging* **13**, 263–274 (1994).
53. Sickles, E. A. Mammographic features of malignancy found during screening. *Recent Results Cancer Res.* **119**, 88–93 (1990).
54. Stavros, A. T. *Breast ultrasound*. Lippincott Williams & Wilkins, Philadelphia, 2004).
55. Chaudhari, M. H. *et al.* Breast tumor vascularity identified by contrast enhanced ultrasound and pathology: initial results. *Ultrasonics* **38**, 105–109 (2000).
56. Kuo, S. J., Hsiao, Y. H., Huang, Y. L. & Chen, D. R. Classification of benign and malignant breast tumors using neural networks and three-dimensional power Doppler ultrasound. *Ultrasound Obstet Gynecol* **32**, 97–102 (2008).
57. Larrue, A. & Noble, J. A. Modeling of errors in Nakagami imaging: illustration on breast mass characterization. *Ultrasound Med. Biol.* **40**, 917–930 (2014).
58. Nowicki, A. *et al.* Differentiation of normal tissue and tissue lesions using statistical properties of backscattered ultrasound in breast. *IEEE Ultrason. Symp. Proc.* **1** (2015).
59. Shankar, P. M. Statistics of boundaries in ultrasonic B-scan images. *Ultrasound Med. Biol.* **41**, 268–280 (2015).
60. Cheng, J. & Beaulieu, N. C. Maximum-likelihood based estimation of the Nakagami m parameter. *IEEE Commun. Lett.* **5**, 101–103 (2001).
61. Tsui, P. H., Ma, H. Y., Zhou, Z., Ho, M. C. & Lee, Y. H. Window-modulated compounding Nakagami imaging for ultrasound tissue characterization. *Ultrasonics* **54**, 1448–1459 (2014).
62. Fujii, Y., Taniguchi, N., Akiyama, I., Tsao, J. W. & Itoh, K. A new system for *in vivo* assessment of the degree of nonlinear generation using the second harmonic component in echo signals. *Ultrasound Med. Biol.* **30**, 1511–1516 (2004).
63. Yeung, R. W. *A first course in information theory*. Kluwer Academic/Plenum Publishers, New York, 2002).
64. Gibbs, V., Cole, D. & Sassano, A. *Ultrasound Physics and Technology: How, Why and When*. Churchill Livingstone, page 70, London, 2009).

Acknowledgements

This work was supported by the Ministry of Science and Technology (Taiwan) under Grant No. MOST 103–2221-E-182–001-MY3 and the Chang Gung Memorial Hospital (Linkou, Taiwan) under Grant Nos CIRPD1E0022, CMRPD1F0311, and CMRPD1C0711.

Author Contributions

P.H.T. and C.K.C. wrote the manuscript text and prepared figures. W.H.K. and K.J.C. worked on clinical experiments. J.F. and H.Y.M. worked on phantom experiments. P.H.T. and H.Y.M. worked on programming. D.C. analyzed data. All authors reviewed the manuscript.

Additional Information

Competing financial interests: The authors declare no competing financial interests.

How to cite this article: Tsui, P.-H. *et al.* Small-window parametric imaging based on information entropy for ultrasound tissue characterization. *Sci. Rep.* **7**, 41004; doi: 10.1038/srep41004 (2017).

Publisher's note: Springer Nature remains neutral with regard to jurisdictional claims in published maps and institutional affiliations.



This work is licensed under a Creative Commons Attribution 4.0 International License. The images or other third party material in this article are included in the article's Creative Commons license, unless indicated otherwise in the credit line; if the material is not included under the Creative Commons license, users will need to obtain permission from the license holder to reproduce the material. To view a copy of this license, visit <http://creativecommons.org/licenses/by/4.0/>

© The Author(s) 2017